Green Synthesis of CdS/Ni$_x$S$_y$ Nanoparticles as a Route Towards Sustainable and Scalable Photocatalysts

Journal:	*Green Chemistry*
Manuscript ID	GC-ART-09-2022-003361.R1
Article Type:	Paper
Date Submitted by the Author:	11-Nov-2022
Complete List of Authors:	Sakizadeh, John; Lehigh University, Chemical and Biomolecular Engineering Cline, Joseph; Lehigh University, Materials Science and Engineering Wolfe, Eva; Lehigh University, Chemical and Biomolecular Engineering Thorpe, Ryan; Lehigh University, Institute for Functional Materials and Devices Snyder, Mark; Lehigh University, Chemical and Biomolecular Engineering Kiely, Christopher; Lehigh University, Materials Science and Engineering; Lehigh University, Chemical and Biomolecular Engineering McIntosh, Steven; Lehigh University, Chemical and Biomolecular Engineering

SCHOLARONE™
Manuscripts

Green Synthesis of CdS/Ni$_x$S$_y$ Nanoparticles as a Route Towards Sustainable and Scalable Photocatalysts

John Sakizadeh[1], Joseph P. Cline[2], Eva Wolfe[1], Ryan Thorpe[3], Mark A. Snyder[1], Christopher J. Kiely[1,2], Steven McIntosh[1]*

[1] Department of Chemical and Biomolecular Engineering, Lehigh University, Bethlehem, PA 18015, USA

[2] Department of Materials Science and Engineering, Lehigh University, Bethlehem, PA 18015, USA

[3] Institute for Functional Materials and Devices, Lehigh University, Bethlehem, PA 18015, USA

*Corresponding author: mcintosh@lehigh.edu

Abstract

If hydrogen evolution photocatalysis are to be deployed at industrial scale, the synthesis of these photocatalytic materials must be both economically and environmentally scalable. This suggests that we must move towards green synthesis of earth-abundant photocatalysts while also maintaining high catalytic performance. Herein, we present the enzymatically driven, aqueous phase, low temperature, synthesis of an earth-abundant nickel sulfide (Ni$_x$S$_y$) hydrogen evolution cocatalyst, and its integration into a CdS/Ni$_x$S$_y$ heterostructured photocatalyst. This resulting photocatalyst provides hydrogen evolution rates (10,500 µmol h^{-1} g^{-1}) comparable to photocatalysts prepared by more traditional routes. Furthermore, the Ni$_x$S$_y$ is demonstrated to provide similar activity enhancement to the more traditional, but also more expensive platinum cocatalysts. To achieve this result, we carefully studied and engineered the synthesis environment to maintain enzyme activity towards HS$^-$ production while sustaining a sufficient concentration of free Ni^{2+} in solution to enable reaction and formation of Ni$_x$S$_y$. Ultimately, this work provides a methodology to control the coordination of metal precursors in low temperature, aqueous systems to allow for precipitation of catalytically active materials and demonstrates the viability of green synthesis pathways for photocatalysts.

Introduction

Photocatalytic hydrogen production from water is a potential clean and renewable process to convert solar to chemical energy. However, the scale at which these materials must be manufactured and deployed for global impact indicates that reliance on complex and unsustainable synthesis routes and precious metal cocatalysts is untenable. The primary

challenge is to overcome these barriers while retaining application-relevant photocatalytic performance. There has been significant research focused on replacing expensive cocatalysts, primarily platinum, with lower-cost, earth-abundant metals such as nickel.[1,2] In particular, nickel sulfides (Ni_xS_y) have emerged as a promising cocatalyst for photocatalytic hydrogen evolution, however, current Ni_xS_y synthesis routes utilize high temperatures, expensive or toxic precursors, and multi-step processing.[3-7] Herein, we demonstrate the low temperature, aqueous enzymatically driven synthesis of an efficient Ni_xS_y hydrogen evolution cocatalyst by controlling the coordination strength of Ni^{2+} and L-cysteine.

One challenge with the production of photocatalysts using alternative, aqueous and low temperature green synthesis routes is to enable material synthesis without employing the high temperatures typically utilized to overcome kinetic barriers. It is thus critical to understand the interactions between metal ions in solution and molecular precursors, like capping and buffering agents, and the effect of these interactions on the thermodynamics and kinetics of the precipitation of particulate photocatalysts. Generally, precipitation of dissolved metal ions in aqueous solution can be initiated by changing pH to form metal oxides or hydroxides, or by introducing reactive sulfur groups, like S^{2-} or HS^-, to form metal sulfides.[8-12] In these low temperature systems, capping agents are typically introduced to improve particle synthesis by providing a template for growth or by controlling product morphology. However, in systems that include both dissolved metal ions and molecular species, complications can arise due to the formation of coordination compounds, which generally increase the entropy of the system, stabilize metal ions, and can preclude particle precipitation.[13,14]

Bio-inspired syntheses have been demonstrated as low temperature, aqueous pathways for photocatalysts, but typically generate even more complexity, such as by introducing strongly chelating biomolecules, compared to conventional syntheses.[15-17] In our group, we have developed the single-enzyme synthesis of CdS-based photocatalysts, where the synthesis system utilizes a minimal set of species in solution: a metal salt, an active enzyme, L-cysteine amino acid as a sulfur source and capping agent, and a buffer to control pH.[18-20] For the enzymatic synthesis of these photocatalysts, we have isolated the enzyme cystathionine γ-lyase (CSE), which steadily catalyzes the decomposition of L-cysteine to form dissolved HS^- species. The slowly generated HS^- species are then capable of reacting with metal ions in solution to grow metal sulfide nanocrystals over time. Excess L-cysteine molecules in solution bind to the surface of the growing metal sulfide nucleates, constraining growth and giving the particles a nanocrystalline morphology. While

the enzymatic synthesis using CSE works well in the case of metals like Cd^{2+}, which do not form stable coordination compounds with moieties required for enzymatic synthesis and readily react with HS^- to form metal sulfides, other metals, like Ni^{2+}, form stable coordination compounds which preclude metal sulfide formation. To expand the accessible materials palette and produce materials like Ni_xS_y, which has typically been produced under harsh reaction conditions, requires an enhanced understanding and control of coordination complex stability in the enzymatic reaction system.[2,21]

In the instance of the enzymatic synthesis of Ni_xS_y by CSE, we hypothesized that the direct precipitation of Ni_xS_y would be unsuccessful due to formation of a stable nickel-L-cysteine (Ni^{2+}-cys) chelation complex under the conditions required to maintain CSE activity.[22,23] Therefore, synthesizing Ni_xS_y using CSE necessitates decreasing the stability of the Ni^{2+}-cys complex. Studies focusing on coordinated metal precursors in the context of particle synthesis are limited; Sun *et al.* and Wark *et al.* have demonstrated the stabilization of metal ions through coordination to delay particle precipitation and promote cation exchange, respectively, but tuning of the coordination strength was not thoroughly investigated.[24,25] In a more relevant study, Yin *et al.* have shown that the kinetics of platinum nanoparticle formation are controlled by the pre-nucleation ligands coordinating platinum ions, but again little insight was offered into limiting or bypassing complexation that may be detrimental to particle precipitation, as is the case for the enzymatic synthesis of Ni_xS_y.[26] However, in the fields of metal-organic frameworks (MOFs) and metal-coordinating polymers, there have been more detailed investigations on controlling product properties by adjusting metal-ligand coordination strength.[27-29] For instance, Huelsenbeck *et al.* have shown that by adjusting the synthesis pH of MOFs, they could control the protonation state of organic linker molecules, and thus tune the coordinating strength of metal ions with organic linkers.[29] Additionally, Holten-Andersen *et al.* have clearly demonstrated control over the viscoelastic properties of a polymer by employing pH to modulate the coordinating strength of catechol groups to Fe^{3+} incorporated within a polymer network.[17] These studies, in combination with prior studies demonstrating the pH-dependent association of Ni^{2+} and L-cysteine, suggest that pH adjustment can be used to control metal-ligand coordination strength in the enzymatic synthesis system to overcome Ni^{2+}-cys complex formation and allow for successful synthesis of Ni_xS_y.[30]

In the first part of this study, we demonstrate that by decreasing the pH of the enzymatic synthesis environment the stability of the Ni^{2+}-cys complex is reduced while still maintaining some CSE activity, thereby allowing for the synthesis of amorphous and aggregated Ni_xS_y. Subsequently, the as-synthesized, aggregated Ni_xS_y is dispersed

onto an enzymatically synthesized CdS hydrogen evolution photocatalyst to enhance the hydrogen evolution activity. The photocatalytic hydrogen evolution rate of the optimized CdS/Ni_xS_y photocatalyst was found to be competitive with reported hydrogen evolution rates of CdS/Ni_xS_y synthesized through high temperature means as well as with enzymatically synthesized CdS with a photodeposited platinum cocatalyst. The high performance of the enzymatically synthesized CdS/Ni_xS_y material demonstrates the viability of low temperature, aqueous syntheses to produce photocatalysts. From a broader perspective, this work provides a facile and rational methodology for controlling molecular interactions to allow for particle precipitation and paves a path for future studies on the low temperature, aqueous synthesis of photocatalysts.

Results & discussion

Controlling coordination of Ni^{2+} in the enzymatic synthesis system

In order to control the Ni_xS_y synthesis, it is first necessary to understand the conditions under which Ni_xS_y precipitates from aqueous solution, and the influence that the enzymatic synthesis solution has on the feasibility of this Ni_xS_y precipitation. It has previously been reported that a Ni_xS_y precipitate forms upon bubbling H_2S through Ni^{2+} solutions under ambient conditions.[31] In our work, a dark precipitate, characteristic of Ni_xS_y, rapidly forms upon direct addition of NaHS to previously pale blue solutions of $Ni(NO_3)_2$ in Tris pH 9 buffer (Figure 1a-b).[32] The ultraviolet-visible (UV-vis) absorbance spectrum of $Ni(NO_3)_2$ in Tris pH 9 buffer has two characteristic absorption peaks at approximately 400 and 700 nm attributed to $Ni(H_2O)_6^{2+}$ and an absorption peak at 300 nm attributed to NO_3^- (Figure 1e).[33,34] The precipitation reaction was also characterized by UV-vis spectroscopy, (Figure 1e), where the characteristic $Ni(H_2O)_6^{2+}$ absorption peaks are now masked by an increase in absorption across the whole visible region, attributable to the formation of black Ni_xS_y.

Ni(NO_3)_2 was then added to solutions of L-cysteine, the sulfur source for the enzymatic reaction, in Tris pH 9 buffer to determine how the enzyme (CSE), L-cysteine, and buffer solution influence the synthesis of Ni_xS_y. Tris pH 9 buffer was used to control pH for optimal CSE enzymatic activity.[30,35] The presence of L-cysteine in the Ni^{2+} solution leads to a color change to reddish brown (Figure 1c) from the pale blue $Ni(NO_3)_2$ solution without L-cysteine (Figure 1a). This color change is accompanied by a decrease in the intensity of the $Ni(H_2O)_6^{2+}$ UV-vis absorption peak, and the appearance of a new absorption peak at 470 nm; both changes are indicative of the formation of a stable Ni^{2+}-cys

complex (Figure 1f).[22] No appreciable change in UV-vis absorption or visible precipitation occurred upon addition of NaHS to these solutions (Figure 1g), indicating that the formation of the stable Ni^{2+}-cys complex inhibits the formation of Ni_xS_y.
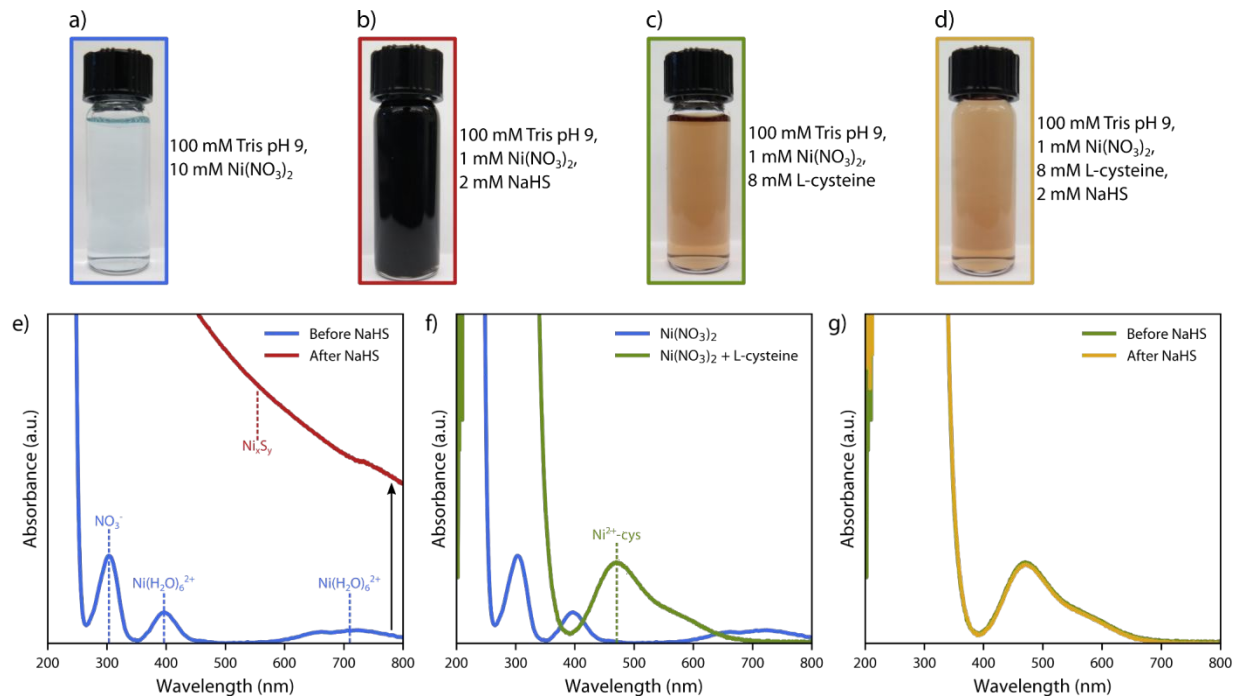
Figure 1. (a-d) Images of $Ni(NO_3)_2$ dissolved in 100 mM Tris pH 9 buffer with and without 8 mM L-cysteine before and after adding 2 mM NaHS in an to attempt to precipitate Ni_xS_y. The sample pictured in Figure 1a used a higher concentration of 10 mM $Ni(NO_3)_2$, rather than the 1 mM $Ni(NO_3)_2$ used for the other samples, to provide a sufficient amount of UV-vis absorption in Figure 1e and Figure **1**f. e) UV-vis absorption spectra of $Ni(NO_3)_2$ in 100 mM Tris pH 9 buffer before and after adding 2 mM NaHS to the solution to precipitate Ni_xS_y. f) UV-vis absorption spectra of $Ni(NO_3)_2$ in 100 mM Tris pH 9 buffer with and without 8 mM L-cysteine. g) UV-vis absorption spectra of 1 mM $Ni(NO_3)_2$ and 8 mM L-cysteine in 100 mM Tris pH 9 before and after adding 2 mM NaHS. The background solvent signal has been subtracted from all spectra.

As L-cysteine is the proposed sulfur source in our precipitation reaction, it is necessary to suppress the formation of this Ni^{2+}-cys complex to realize Ni_xS_y synthesis. Lubes *et al.* have demonstrated through potentiometric titrations that solutions of Ni^{2+} and L-cysteine at pH ≥ 6.5 favor Ni^{2+}-cys complexation, whereas the same solutions at pH ≤ 6.5 favor free Ni^{2+} ions.[30] Based on this report, a Ni_xS_y precipitation assay was performed by adding NaHS to

solutions of $Ni(NO_3)_2$, L-cysteine and CSE with pH controlled by Tris pH 9, Tris pH 7, and acetate pH 5 buffers. Acetate buffer was used to control the pH under acidic conditions as Tris is only effective at buffering roughly in the 7-9 pH range. The UV-vis spectra of the Ni^{2+}-cys chelation complex are unchanged upon addition of NaHS at pH 9 and 7 (Figure 1g and Figure 2a, respectively, being dominated by the Ni^{2+}-cys complex absorption peak at 470 nm). In contrast, at pH 5 the UV-vis spectrum before NaHS addition shows peaks indicative of both free Ni^{2+} (~400 nm), and the Ni^{2+}-cys complex (470 nm) (Figure 2b). Following addition of NaHS, the UV-vis absorption increased broadly, and a dark precipitate formed, indicating the formation of Ni_xS_y (Figure 2b). These results confirm that by decreasing the pH of the buffer solution, the affinity for Ni^{2+}-cys chelation is decreased, and Ni_xS_y can be precipitated. Desrochers *et al.* have shown that deprotonation of the thiol group of cysteine enhances nickel binding.[36] Since the thiol group on cysteine has a pK_a of 8.4, it would be protonated at pH 5, leading to unchelated Ni^{2+} that can react with HS^- to form Ni_xS_y.[37]
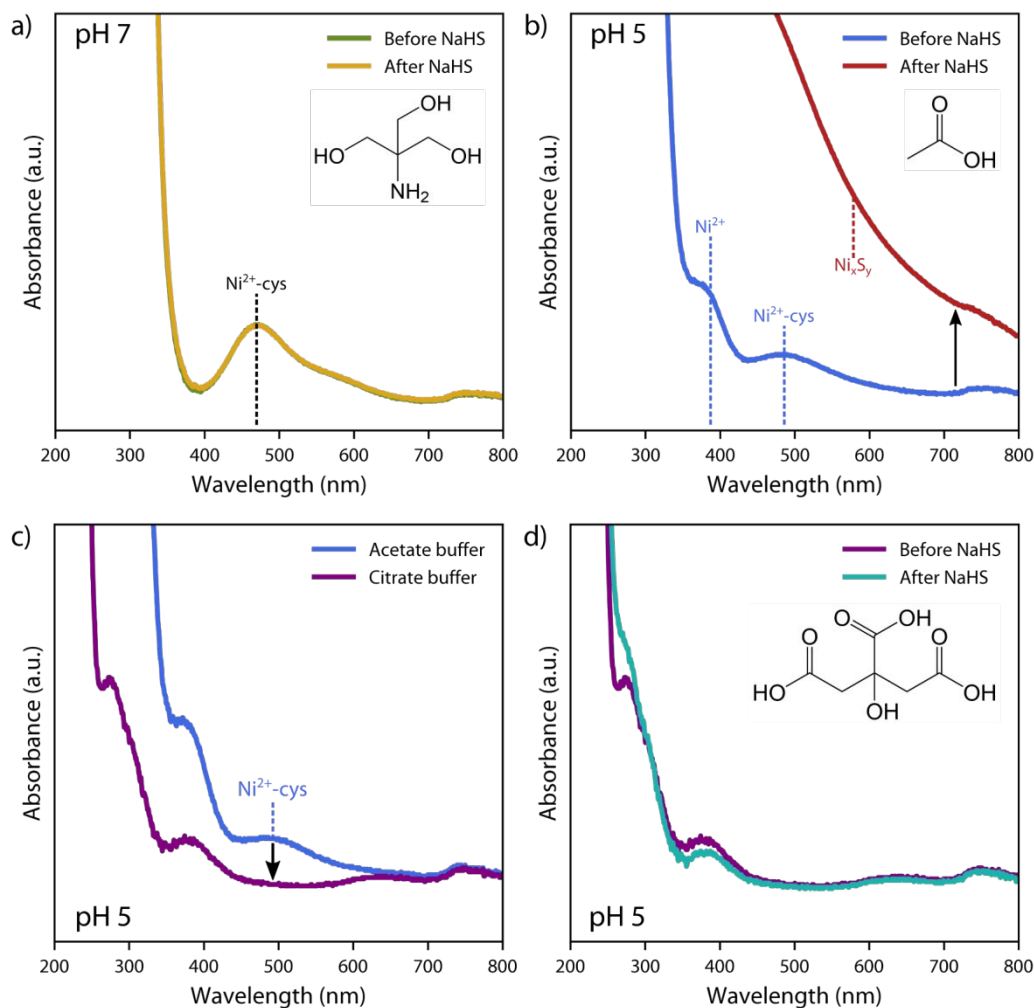
Figure 2. UV-vis absorption spectra of 8 mM L-cysteine, 1 mM Ni(NO$_3$)$_2$, and 0.1 mg mL^{-1} CSE in 100 mM with a) Tris pH 7 and b) pH 5 acetate buffers before and after adding 2 mM NaHS to the solution. c) UV-vis absorption spectra of 8 mM L-cysteine, 1 mM Ni(NO$_3$)$_2$, and 0.1 mg mL^{-1} CSE in pH 5 acetate and citrate buffers. d) UV-vis absorption spectra of 8 mM L-cysteine, 1 mM Ni(NO$_3$)$_2$, and 0.1 mg mL^{-1} CSE in pH 5 citrate buffer before and after adding 2 mM NaHS to solution. The molecules shown inset in a), b), and d) depict the structure of the buffering compounds used for each experiment.

When shifting pH, one must also consider the pH-dependency of the activity of the HS$^-$ producing CSE enzyme. The activity of CSE is reported to diminish as the solution deviates from the often-reported optimal value of pH ~8.[35,38] Additionally, our enzymatic process has only previously been demonstrated in the pH range of 7-9.[39] To determine if CSE is active below this pH range, CSE activity was screened by confirming the generation of HS$^-$ by a qualitative lead-

based assay.[40] The assay results (Figure S1) suggest that while the activity level at pH 5 is somewhat lower, the enzyme is still able to turn over L-cysteine to form reactive HS$^-$. Thus, the presence of sufficiently unchelated Ni^{2+} and persistence of CSE activity at pH 5 underscores the feasibility of Ni$_x$S$_y$ synthesis under these conditions.

One final consideration is the possible coordination of metal precursors by the buffering compound, something that has been a challenge in biosynthesis research, as noted by Good et $al.$, and is an issue in the precipitation of particles through stabilization of dissolved metal ions.[41] In our case, we investigated the role of the denticity of the buffer used in the enzymatic synthesis and its effect on the stability of the dissolved Ni^{2+}, and thus the precipitation of Ni$_x$S$_y$. In general, the higher the denticity of a ligand, the more stable the metal-ligand complex.[14] The acetate used in the pH 5 buffer behaves as a monodentate ligand when binding to Ni^{2+}. Tridentate citrate will bind more strongly to Ni^{2+}; indeed nickel-acetate and nickel-citrate complexes have been reported to be approximately -4 and -31 kJ mol^{-1} more stable than dissolved Ni(H$_2$O)$_6$$^{2+}$, respectively.[42,43] This increased binding strength leads to the avoidance of N^{2+}-cys complex formation, indicated by the absence of an absorbance peak at 470 nm, when utilizing citrate buffer (Figure 2c) in place of acetate buffer (Figure 2b). Unfortunately, addition of NaHS to solutions of L-cysteine, Ni(NO$_3$)$_2$, and citrate buffer (Figure 2d) leads to no change in the UV-vis spectrum, indicating that the tighter binding of citrate to Ni^{2+} suppresses Ni$_x$S$_y$ formation. The inability to form Ni$_x$S$_y$ in the pH 5 citrate buffer highlights the importance of considering the chemical structure of the buffer and its role as a stabilizing agent for metal ions when synthesizing nanocrystals under low temperature, aqueous conditions.

Enzymatic synthesis of Ni$_x$S$_y$

Enzymatic synthesis of Ni$_x$S$_y$ in pH 5 acetate buffer was carried out at 37 °C with an incubation time of 4 h. A black flocculate was formed during incubation and was accompanied by an increase in the UV-vis absorbance (Figure 3) over the entire visible region. This is analogous to the increase in the absorbance upon Ni$_x$S$_y$ formation by adding NaHS to a solution of Ni^{2+} (Figure 1e and Figure 2b). The aggregated nature of the as-synthesized nickel sulfide precipitate suggests the need for further dispersion of nickel sulfide onto a suitable support material before catalytic testing. The mass concentration of Ni$_x$S$_y$ formed was measured by inductively coupled plasma optical emission spectroscopy (ICP-OES) to be 4.6 mg L^{-1}. The successful enzymatic precipitation of Ni$_x$S$_y$ indicates that CSE is capable of catalyzing the decomposition of L-cysteine in the acetate buffer, producing HS$^-$ that then reacts with free Ni^{2+} to form the solid product.
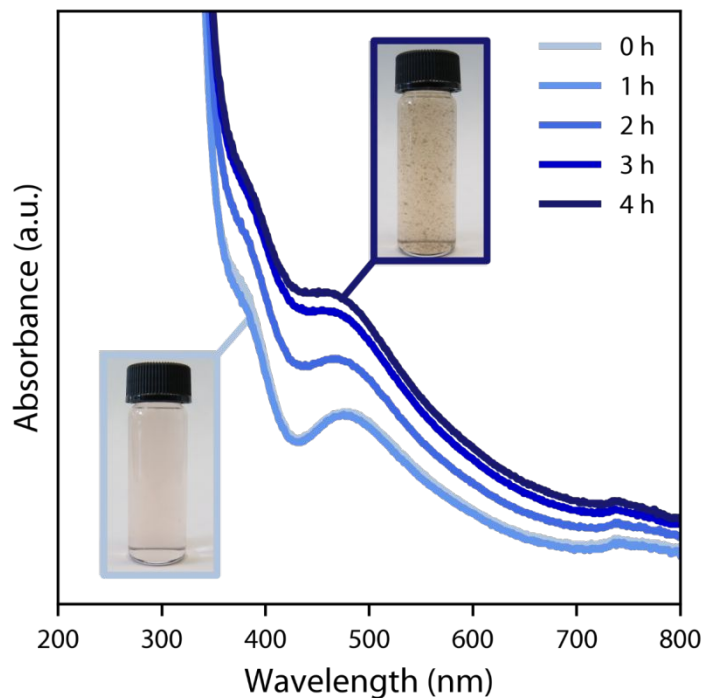
Figure 3. UV-vis absorption spectra of 8 mM L-cysteine, 1 mM Ni(NO$_3$)$_2$, and 0.1 mg mL^{-1} CSE in 100 mM pH 5 acetate buffer after incubating at 37 °C for a designated amount of time between 0 and 4 h. Inset images of the enzymatic synthesis solution before and after 4 h of incubation at 37 °C show the formation of a dark precipitate.

Unlike our previous reports of enzymatic syntheses at higher pH, a critical parameter in this synthesis of Ni$_x$S$_y$ was whether the synthesis vessel was open or closed. When leaving the reaction vessel open, a less pronounced increase in the absorbance signal across the UV-vis spectrum was observed (Figure S2). H$_2$S has a pK$_a$ of 6.99, so HS$^-$ is prone to accept a proton under the acidic conditions of the pH 5 acetate buffer used in this study, and is therefore more likely to exist as H$_2$S, which can transport out of an open reaction vessel.[44] For this reason, our Ni$_x$S$_y$ synthesis was performed in a sealed container with minimal headspace.

Structure and morphology of the enzymatically synthesized Ni$_x$S$_y$

High angle annular dark-field (HAADF) imaging in a scanning transmission electron microscope confirmed the enzymatic synthesis of an amorphous Ni$_x$S$_y$ material (Figure 4a). The Ni$_x$S$_y$ was found to be highly agglomerated with a

primary particle size on the order of 10 nm diameter. Energy dispersive x-ray spectroscopy (XEDS) confirmed the presence of nickel and sulfur in the particles (Figure 4b).
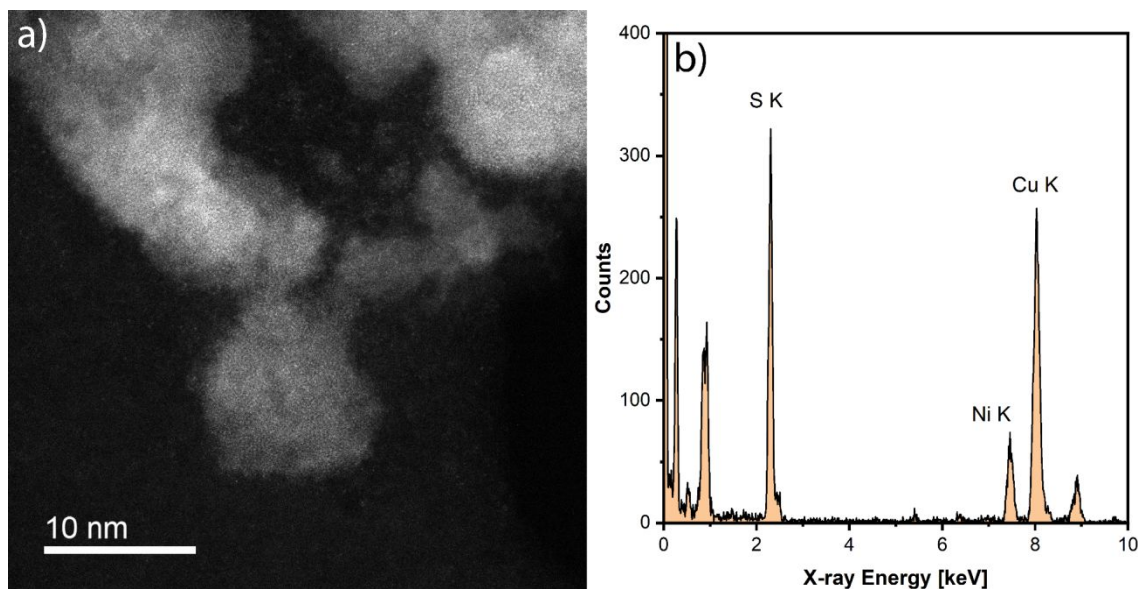
Figure 4. a) HAADF-STEM micrographs of enzymatically synthesized Ni_xS_y and b) accompanying XEDS spectra.

Prior studies on the preparation of Ni_xS_y nanoparticles strongly suggest that lower temperature syntheses favor amorphous Ni_xS_y while higher temperature syntheses have been shown to generate crystalline forms.[45] For the enzymatic process, there is only a very limited degree of control over the synthesis temperature as the CSE enzyme is active at 37 °C with a small functional window on either side, thus the enzymatically synthesized Ni_xS_y was expected to be amorphous in character.[39] The amorphous Ni_xS_y product by itself was found to be inactive for photocatalytic hydrogen evolution, as expected, due to its small band gap (Figure S3).[46] Yet, given that amorphous Ni_xS_y has previously been shown to improve hydrogen evolution performance as a cocatalyst for metal sulfide photocatalysts,[47] the pre-formed Ni_xS_y material can be used as a precursor for the formation of Ni-enriched CdS photocatalysts.

Enhanced photocatalytic hydrogen evolution from enzymatically synthesized Ni_xS_y/CdS catalyst materials

The enzymatically synthesized Ni_xS_y was incorporated onto a nanocrystalline CdS hydrogen evolution photocatalyst to test its capability to further enhance the hydrogen evolution rate of the CdS material. The CdS nanocrystals were enzymatically synthesized by incubating CSE, L-cysteine, and Cd^{2+} in Tris pH 9 buffer at 37 °C for 4 h, as reported

elsewhere.[20] To incorporate the Ni_xS_y onto CdS, the enzymatically synthesized Ni_xS_y material was centrifuged and washed to remove buffer, CSE, and any residual precursors prior to addition to the stable CdS sol. Between 0 and 5 wt-% Ni_xS_y was added to the CdS. It should be noted that the synthesis of CdS nanocrystals requires an alkaline pH level. As such, a one pot enzymatic synthesis of a CdS/Ni_xS_y photocatalyst was not possible as under alkaline conditions the Ni^{2+} would remain in solution in the form of a Ni^{2+}-cys complex, as previously discussed, and not be efficiently incorporated into the CdS crystal lattice.

HAADF-STEM imaging and XEDS mapping of the CdS/Ni_xS_y material revealed the existence of both the wurtzite and zincblende forms of CdS and the presence of Ni within these CdS particles, suggesting that the nickel has redispersed across the CdS (Figure 5 and Figure S4). Note that we typically find mixtures of wurtzite and zincblende CdS nanoparticles from the enzymatic synthesis route. The low XEDS signal of Ni in Figure 5 and Figure S4b is attributable to the low (2.7 wt-%) concentration of Ni_xS_y in the CdS/Ni_xS_y catalyst. Furthermore, large aggregates of Ni_xS_y (as seen in Figure 4a) were not observed during collection of any micrographs of the CdS/Ni_xS_y material, further suggesting that the Ni_xS_y has redistributed across the CdS. The change in Ni_xS_y from the as-synthesized agglomerated particle morphology (Figure 4a) to a more uniform dispersion of the Ni_xS_y over the CdS is attributed to the unstable nature of the enzymatically synthesized Ni_xS_y in aqueous environments.
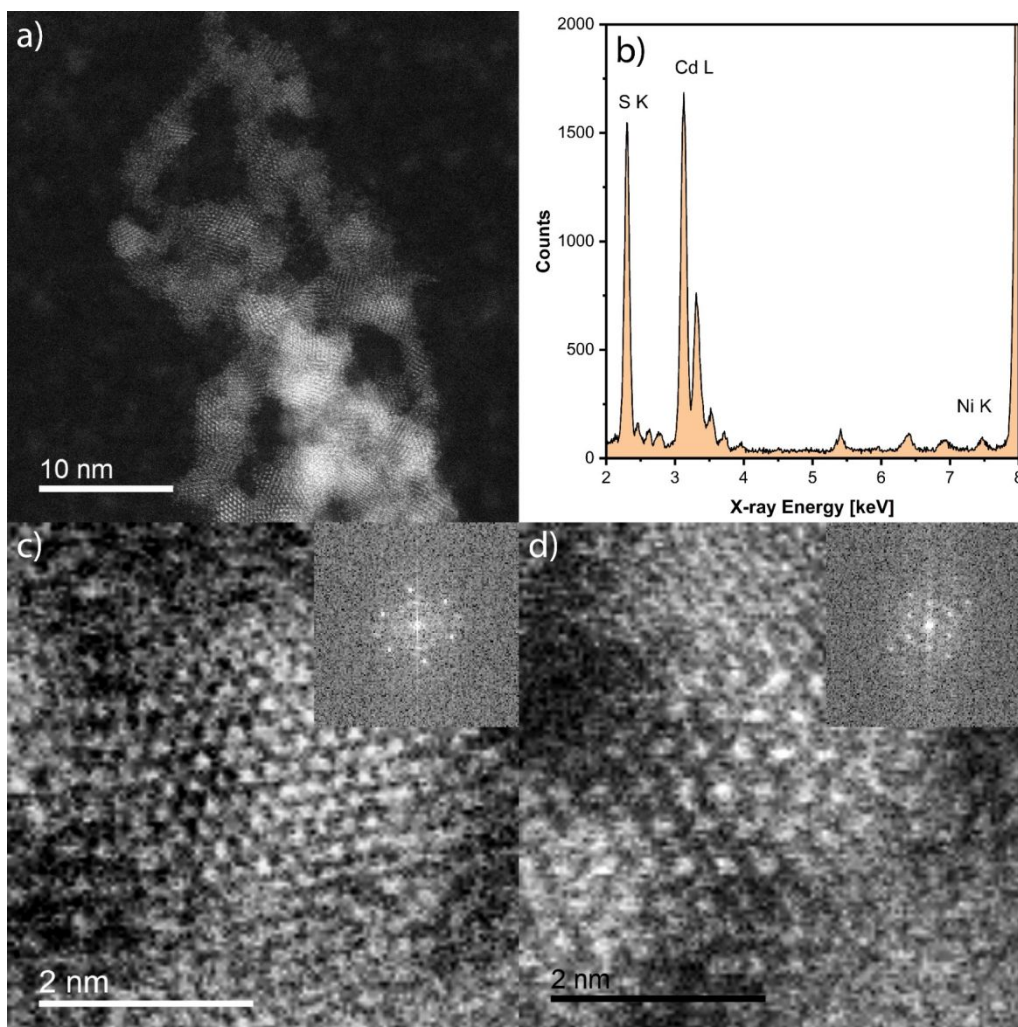
Figure 5. a) Representative low magnification HAADF-STEM image of CdS/Ni$_x$S$_y$ with 2.7 wt-% Ni$_x$S$_y$ and b) the corresponding XEDS spectrum. High magnification HAADF-STEM images of individual CdS particles fitted to c) zincblende and d) wurtzite-type polymorphs. The FFT insets in c) and d) correspond to the [111] and [001] directions in cubic sphalerite and hexagonal wurtzite CdS polymorphs respectively.

The change in morphology of Ni$_x$S$_y$ under different environmental conditions was investigated using UV-vis spectroscopy. Because Ni$_x$S$_y$ absorbs and scatters light across the visible and near IR regions, a larger increase in absorbance in these regions qualitatively corresponds to a larger and/or higher concentration of Ni$_x$S$_y$ particles. Figures S5 and S6 show the absorbance at 800 nm of a suspension of biomineralized Ni$_x$S$_y$ under photocatalytic testing conditions (100 mM Na$_2$S, 100 mM Na$_2$SO$_3$, 50 mM Tris pH 9 buffer, and 4 mM L-cysteine) as a function of time. The progressive decrease in absorbance at 800nm with time demonstrates the gradual dissolution of the Ni$_x$S$_y$. The

dissolution of Ni_xS_y can be explained by the pH of the Ni_xS_y suspension environment. The photocatalytic testing environment had an alkaline pH, and in prior experiments alkaline (Figure 1g) and even neutral pH (Figure 2a) has been demonstrated to limit Ni_xS_y particle formation in the presence of L-cysteine. Limited Ni_xS_y particle formation in neutral pH in the presence of L-cysteine additionally explains the observation of uniformly dispersed Ni_xS_y on CdS in HAADF-STEM images (Figure 5) and accompanying XEDS mapping (Figure S4) of samples formed by simply mixing CdS and Ni_xS_y in unbuffered aqueous solutions containing residual L-cysteine at near neutral pH. Therefore, the initially large, aggregated biomineralized Ni_xS_y acts as a nickel source for the formation of dispersed Ni_xS_y on CdS. This dispersion of Ni_xS_y onto CdS is desirable given its concomitant enhancement of the surface-area-to-volume ratio of the cocatalyst in close contact with the CdS, which enables more efficient transfer of photogenerated intermediates.

High-resolution X-ray photoelectron spectroscopy (XPS) was used to confirm the presence of nickel, cadmium, and the expected metal sulfide moieties in the CdS/Ni_xS_y sample (Figure 6a-c). The XPS spectrum of the Cd *3d* region exhibits peaks with binding energies at 404.1 and 410.8 eV and the spectrum of the Ni *2p* region displays peaks at 854.9, 873.0, 861.2, and 878.3 eV, which are consistent with prior reports for CdS and Ni_xS_y, respectively.[48,49] The XPS spectra of the S *2p* region reveals peaks at 161.4 and 162.7 eV, attributed to Ni_xS_y, as well as at 160.2 and 161.4 eV, attributed to CdS (Figure 6c).[50,51] The presence of Ni_xS_y signal in the S *2p* region demonstrates that Ni_xS_y is present despite the morphological change of the material. The peaks in the S *2p* spectra at 162.5 and 163.66 eV are associated with thiol groups, most likely originating from surface capping L-cysteine ligands.[52]
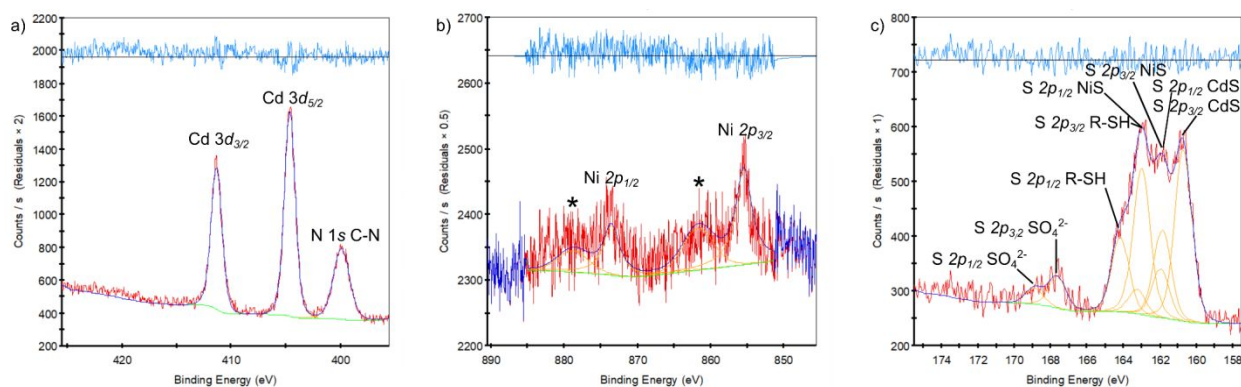
Figure 6. High-resolution XPS spectra of the a) Cd *3d*, b) Ni *2p*, and c) S *2p* regions from a CdS-2.7 wt-% Ni_xS_y sample. The peaks in b) marked with an asterisk are attributed to satellite peaks that often appear for nickel-based materials.**[49]**

The hydrogen evolution rate of the as-synthesized CdS/Ni_xS_y sample is compared to that of bare CdS nanocrystals in Figure 7a, and as a function of the added wt-% amount of Ni_xS_y (Figure 7b). The hydrogen evolution rate of CdS/Ni_xS_y increases as the wt-% of Ni_xS_y in the system increases, until the weight percentage reaches an optimum value of 2.7 wt% at which point a reaction rate of 10,500 $\mu mol\ h^{-1}\ g^{-1}$ is achieved representing a seven-fold increase in hydrogen evolution rate when compared to bare CdS (~1,400 $\mu mol\ h^{-1}\ g^{-1}$). Beyond this optimum Ni_xS_y loading, the hydrogen evolution rate decreased. Zhou *et al.* and Chen *et al.* have shown similar trends in the hydrogen evolution rate as the amount of Ni_xS_y reaches and surpasses an optimum value, an effect which has been attributed to the occlusion of light caused by the presence of too much absorptive Ni_xS_y.[3,4] However, in our case the concentration of Ni_xS_y was low and thus its influence on CdS light absorption was considered negligible; therefore, the optimum in the hydrogen evolution rate of CdS with Ni_xS_y loading was possibly due to inefficient dispersion of Ni_xS_y at higher loadings, as has been investigated in other catalyst performance studies.[53] We calculate that, if fully dispersed, the optimal loading of 2.7 wt-% Ni_xS_y would create a surface coverage of around 30-40%. It appears that the increase to 3.5 wt-% may lead to non-optimal CdS surface coverage by Ni_xS_y. Furthermore, when enzymatically synthesized Ni_xS_y was tested for photocatalytic hydrogen production in the absence of CdS, no hydrogen was produced (Figure S3), indicating the enhancement in the hydrogen evolution rate of CdS with Ni_xS_y is not due to Ni_xS_y behaving as a hydrogen evolution photocatalyst independent of CdS. Rather, Ni_xS_y acts as a synergistic cocatalyst for hydrogen evolution when paired with CdS in this manner.
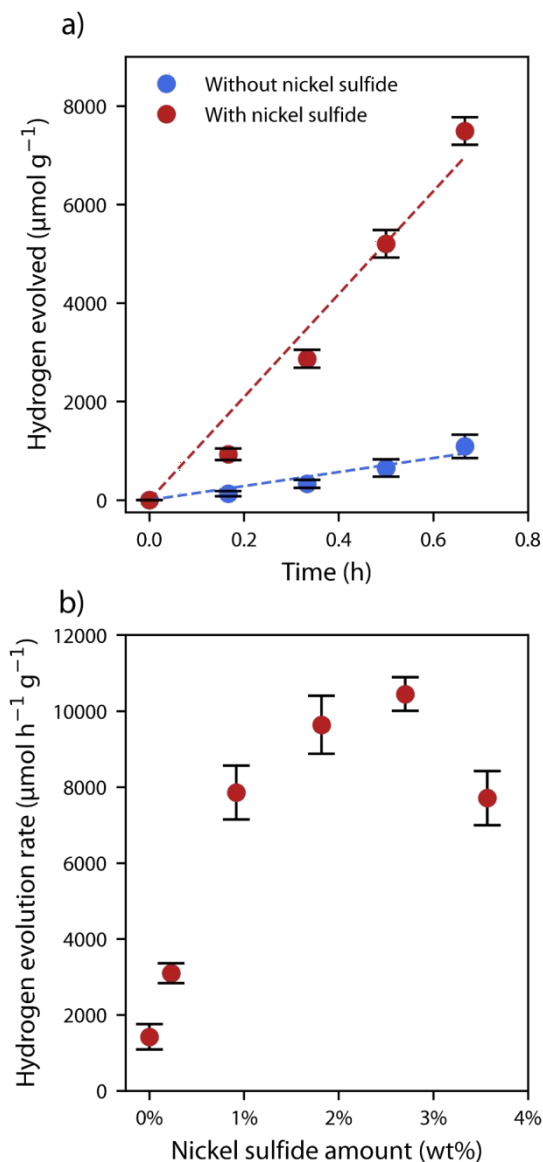
Figure 7. a) Photocatalytic hydrogen evolution over pure CdS nanocrystals as compared against the CdS nanocrystals associated with 2.7 wt-% Ni_xS_y. b) Photocatalytic hydrogen evolution rates of CdS nanocrystals with controlled varying amounts of Ni_xS_y added to the system. The optimum amount of Ni_xS_y to add to the CdS nanocrystals was determined to be 2.7 wt-%. Tabulated hydrogen rate values for all the photocatalysts tested are presented in Table S1.

Past studies of CdS/Ni_xS_y hydrogen evolution photocatalysts synthesized through more conventional preparation methods have typically reported hydrogen evolution rates between 1,500-30,000 µmol h^{-1} g^{-1}, with one outlying report claiming a rate as high as 400,000 µmol h^{-1} g^{-1} (Table S2). Thus, hydrogen production rates from our

enzymatically synthesized photocatalyst (10,500 μmol h^{-1} g^{-1}) are competitive with those achieved by more traditional synthesis routes. Additionally, we have demonstrated that, through careful consideration of synthesis and processing parameters, aqueous phase, room temperature, enzymatic synthesis is a viable alternative route for the production of these heterostructured photocatalysts.

Our enzymatic synthesis of Ni$_x$S$_y$ cocatalysts required an aqueous environment with temperatures of 37 °C for a duration of 4 h, while other reported syntheses of Ni$_x$S$_y$ cocatalysts used temperatures between 120-200 °C for 4-24 h[3-7] or the use of the sacrificial reagent as the reactive sulfur precursor[47,54]. Additionally, the enzymatic synthesis conditions for the CdS component of the catalyst (also 37 °C for 4 h in an aqueous environment) had a lower temperature and relatively short reaction time in comparison to the conventional laboratory synthesis methods for CdS, which predominately employ temperatures between 160-200 °C for 4-24 h.[3-7,47,54]

In terms of the operational stability of our CdS/Ni$_x$S$_y$ catalyst, the hydrogen evolution rate of the sample with the optimal Ni$_x$S$_y$ loading decreased after 2 h of testing (Figure S7). This degradation in performance is common with metal sulfide photocatalysts, and in this case was attributed to photooxidation, where photogenerated holes on CdS oxidize metal lattice sites causing degradation of the photocatalyst.[55]

While there are limited studies on the underlying mechanistic causes for the observed enhancement in the hydrogen evolution rate when using Ni$_x$S$_y$ as a cocatalyst, DFT studies on platinum-based electrocatalysts and metal sulfide-based photocatalysts suggest that using a cocatalyst for hydrogen evolution lowers the activation barrier for water dissociation, which is hypothesized to be the rate limiting step in the hydrogen evolution mechanism.[56,57] Zhou *et al.* and Chen *et al.* suggest that Ni$_x$S$_y$ improves the photocatalytic hydrogen production rate of CdS by accepting photoexcited electrons.[3,4] It was suggested that photoexcited electrons transfer from the CdS conduction band to Ni$_x$S$_y$ where the hydrogen evolution reaction occurs.[3,4,58] DFT studies by Zhao *et al.* support this hypothesis, suggesting that electrons in the conduction band of a CdS-based photocatalyst are at a higher energy than the conduction band of Ni$_x$S$_y$, thus promoting electron transfer.[56] Furthermore, band gap measurements of CdS with and without Ni$_x$S$_y$ show that including Ni$_x$S$_y$ decreases the magnitude of the band gap and suggests the introduction of an energy level into which a photoexcited electron can be transferred from the conduction band.[56]

Comparison between Ni$_x$S$_y$ and Pt cocatalysts with CdS

Comparing the mass normalized hydrogen evolution rates of the enzymatically synthesized CdS/Ni$_x$S$_y$ to other reports of similar photocatalysts in the literature is useful, but ultimately is always an approximation due to uncontrolled system variables between reported experiments.[59] To further demonstrate the viability of Ni$_x$S$_y$ as a cocatalyst, an additional comparison was performed to an enzymatically synthesized CdS sample which used platinum as a cocatalyst. Platinum is conventionally regarded as the most efficient metal cocatalyst for hydrogen evolution.[60]

Platinum was photodeposited (from chloroplatinic acid hexahydrate) onto CdS by exposing the sample to the full lamp spectrum for 10 min. Photodepositing the platinum for longer periods of time, caused a decay in the photocatalytic hydrogen evolution rate, most likely due to photocorrosion of the CdS under full spectrum illumination (Figure S8). Hydrogen evolution rates over the CdS/Pt sample were measured with different platinum loadings, finding an optimum at 5 wt-% Pt (Figure 8a). This agrees with the results of prior studies of CdS/Pt systems that show that hydrogen evolution rate is optimized by controlling the loading of platinum on CdS.[61,62] HAADF-STEM imaging of the CdS/Pt samples confirms the presence of occasional f.c.c. platinum nanoparticles (Figure S9). It is possible that atomically dispersed platinum exists alongside the observed platinum nanoparticles, however, it was difficult to detect this in our electron microscopy or XEDS studies due to the low concentration of photodeposited platinum. The hydrogen evolution rate of CdS with 5 wt-% platinum, at 3,400 µmol h^{-1} g^{-1}, was lower than the rate achieved with the optimal amount of Ni$_x$S$_y$, added to CdS of 10,500 µmol h^{-1} g^{-1}.

While other studies have compared the performance of CdS/Ni$_x$S$_y$ to CdS/Pt, it is important, although not practiced, to control for possible degradation in the photocatalyst performance of the CdS component that may take place during the platinum photodeposition step due to photocorrosion.[7,47] To account for this in our work, an enzymatically synthesized CdS sample was exposed to the full lamp spectrum for 10 min before adding 2.7 wt-% Ni$_x$S$_y$. When taking this photocorrosion effect into account, the hydrogen evolution rate of the CdS/Ni$_x$S$_y$ sample at 4,400 µmol h^{-1} g^{-1} was comparable to the hydrogen evolution rate of CdS/Pt, 3,400 µmol h^{-1} g^{-1}, and demonstrates that Ni$_x$S$_y$ is highly competitive with platinum as a cocatalyst. (Figure 8b-c).
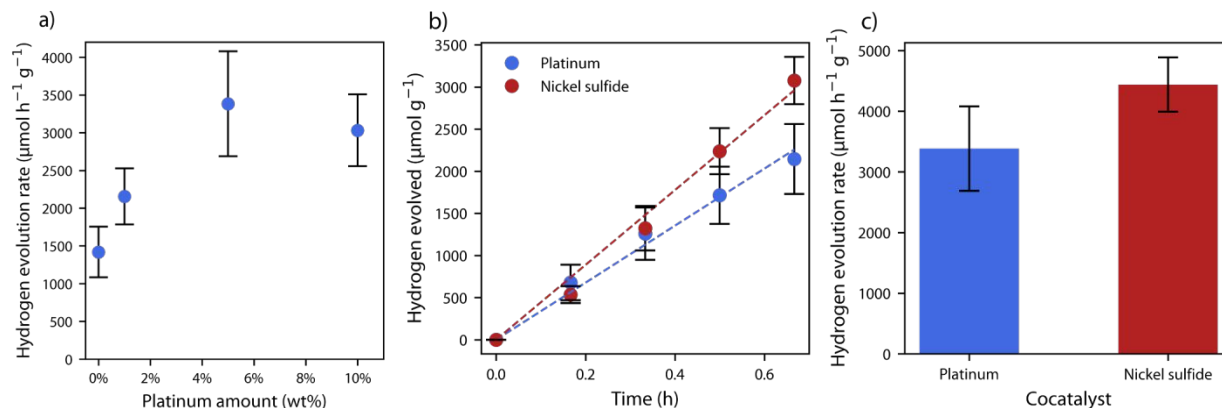
Figure 8. a) Photocatalytic hydrogen evolution rates of CdS nanocrystals with varying amounts of chloroplatinic acid hexahydrate added to the system before photodeposition. The optimum amount of platinum to add to CdS nanocrystals was determined to be 5 wt-%. b) Photocatalytic hydrogen evolution of enzymatically synthesized CdS nanocrystals with 5 wt-% platinum after a 10 min photodeposition period (blue line) as compared with enzymatically synthesized CdS nanocrystals exposed to photodeposition conditions for 10 min before introduction of 2.7 wt-% of enzymatically synthesized Ni_xS_y. c) Photocatalytic hydrogen evolution rates obtained from b) by fitting data to a linear model. Tabulated hydrogen rate values for all CdS/Pt photocatalysts are presented in Table S3.

The hydrogen evolution rates reported in this text were normalized by the total mass of the photocatalyst. However, it should be noted that mass normalized hydrogen evolution rates can be subject to a host of complicating issues including a non-linear correlation between the hydrogen evolution rate and the photocatalyst mass, as well as the mass normalized rate not taking catalyst geometry into account.[63-65] While the total mass of the photocatalyst and the size/optical properties were kept constant throughout the reported experiments, it is useful to present several rate reporting metrics, as detailed by Fornasiero *et al.*, to ensure they support claims related to the observed hydrogen evolution rate enhancement.[65] In accordance with this, the raw hydrogen evolution reaction rates, the surface area normalized hydrogen evolution reaction rates, and the turnover frequencies of the optimal catalysts are reported in Table S4. These values stand in agreement with our findings that the enzymatically synthesized Ni_xS_y cocatalyst is highly competitive with the conventional photodeposited platinum cocatalyst.

Conclusions

Ni_xS_y has been successfully synthesized through a low temperature, aqueous enzymatic route by tuning the system pH to limit intermolecular interactions detrimental to Ni_xS_y precipitation. It was determined that using an acetate buffer for the enzymatic synthesis with a lower-than-normal pH of 5 reduced the thermodynamic stability of Ni^{2+}-cys chelation complexes, promoting free Ni^{2+} and facilitating its reaction with HS^- that is critical for precipitating Ni_xS_y. Simultaneously, under the buffer pH, CSE remains sufficiently active for producing HS^- by catalyzing the decomposition of L-cysteine. It was found that using a high denticity, pH 5 citrate buffer instead of a lower denticity, pH 5 acetate buffer could also stop precipitation of Ni_xS_y, highlighting the importance of considering buffer chemical structure in such low temperature, aqueous syntheses. The enzymatic synthesis of Ni_xS_y was thus performed in pH 5 acetate buffer, and Ni_xS_y formation was confirmed by HAADF-STEM imaging, XEDS, and ICP-OES analysis. The enzymatically synthesized Ni_xS_y, which was initially aggregated, could be dispersed as a cocatalyst onto a CdS hydrogen evolution photocatalyst, made through a similar enzymatic method, in order to enhance the overall photocatalytic hydrogen evolution rate of CdS. CdS performance was optimized with addition of 2.7 wt-% of Ni_xS_y cocatalyst, improving the hydrogen evolution rate from 1,400 μmol h^{-1} g^{-1} for bare CdS to 10,500 μmol h^{-1} g^{-1} with 2.7 wt-% Ni_xS_y. The photocatalytic hydrogen evolution rate of the optimized enzymatically synthesized CdS/Ni_xS_y catalyst was found to be competitive with reports of CdS/Ni_xS_y produced through harsher, higher temperature methods. The performance of the optimized, enzymatically synthesized CdS/Ni_xS_y was also found to outperform an optimized CdS/Pt sample, even when taking into account photocorrosion of CdS during the photodeposition of platinum. Thus, by rationally designing the low temperature, aqueous synthesis environment, it was possible to successfully synthesize a high-performing Ni_xS_y hydrogen evolution cocatalyst using an enzymatic pathway. The fundamental understanding of important intermolecular interactions and design principles gained in this study has the potential to serve as a blueprint for developing future low temperature, aqueous synthesis pathways for other photocatalysts.

Experimental

Enzymatic synthesis of CdS nanocrystals

L-cysteine-capped CdS nanocrystals were enzymatically synthesized by incubating 1 mM cadmium acetate (Alfa Aesar, 99.999% Puratronic) with 0.5 mg mL^{-1} CSE and 8 mM L-cysteine (Spectrum Chemical, 98%) in a 100 mM Tris buffered (pH 9) solution at 37 °C. As we have previously demonstrated,[66] these conditions promote the enzymatic turnover of L-

cysteine by CSE to generate reactive HS$^-$ species that can then react with Cd^{2+} in solution to form CdS nanocrystals. Size control of the nanocrystals is achieved via the relatively slow and constant generation of HS$^-$ species which serves to keep the nanocrystal growth mechanism within the size-focusing regime throughout the 4 h growth period.[11] The growing nanocrystals are capped by the dissociated thiol groups of unreacted L-cysteine, both stabilizing the crystals in solution and acting to further control particle growth. The enzymatically synthesized CdS nanocrystals used for our experiments had a UV-vis absorption peak at 390 nm with an absorption measured to be 1.4, corresponding to a particle concentration of 5 μM.[67] Before photocatalytic testing, the CdS nanocrystals were precipitated by mixing with ethanol, centrifuged, and resuspended in fresh 100 mM Tris pH 9 buffer with 8 mM L-cysteine.

Ni$_x$S$_y$ precipitation assay

For the Ni$_x$S$_y$ precipitation assay, 1 mM of NaHS was added to solutions of 1 mM Ni(NO$_3$)$_2$, 8 mM L-cysteine, and 0.1 mg mL^{-1} CSE. The solution pH was controlled by either 100 mM of Tris pH 9, Tris pH 7, pH 5 acetate, or pH 5 citrate buffer. UV-vis spectroscopy was used to characterize the formation of Ni$_x$S$_y$ whereby an increase in the UV-vis absorbance in the visible region indicated successful Ni$_x$S$_y$ formation.

Lead acetate assay for screening CSE activity

8 mM L-cysteine and 0.05 mg mL^{-1} CSE in 100 mM Tris pH 9, Tris pH 7, and pH 5 acetate buffers were allowed to incubate at 37 °C for 2 h. The incubation period was followed by the addition 1 mM lead acetate to the CSE/L-cysteine buffered solution, which reacts with dissolved HS$^-$ species generated by CSE turning over L-cysteine to form a brown lead sulfide precipitate that was assayed by UV-vis spectroscopy,[40] and is stable in the proposed pH range used in this study.[68]

Enzymatic synthesis of Ni$_x$S$_y$ nanoparticles and formation of CdS/Ni$_x$S$_y$ catalysts

Ni$_x$S$_y$ nanoparticles were enzymatically synthesized by incubating 1 mM nickel nitrate hexahydrate (Alfa Aesar, 99.9985%) with 0.1 mg mL^{-1} CSE and 8 mM L-cysteine (Spectrum Chemical, 98%) in a 100 mM acetate buffered (pH 5) solution at 37 °C for 4 h. The amount of headspace above the solution in the glass vial used to carry out the enzymatic synthesis of Ni$_x$S$_y$ nanoparticles was minimized by filling the entire vial with liquid, which is important to limit the loss

of dissolved HS= through transport of H_2S into the surrounding atmosphere. The Ni_xS_y nanoparticles subsequently were centrifuged out of solution and resuspended in DI water. The formation of the CdS/Ni_xS_y catalyst was performed by adding a specific wt-% amount of Ni_xS_y to the washed enzymatically synthesized CdS nanocrystals that were resuspended in fresh 100 mM Tris pH 9 buffer with 8 mM L-cysteine.

Synthesis of CdS/Pt catalysts through photodeposition

For samples with a platinum co-catalyst, the platinum component was photodeposited by adding 0-10 wt-% of Pt to the CdS sol through addition of the appropriate amount of chloroplatinic acid hexahydrate (Sigma-Aldrich, 99.995%) to the CdS photocatalyst in a 0.1 M Na_2S/0.1 M Na_2SO_3 sacrificial reagent. The mixture was then irradiated for 30 min using an unfiltered 350 W Xenon lamp situated 20 cm away from the sample, followed by purging the system with N_2 before any further testing.

Photocatalytic H_2 generation

Photocatalyst samples were tested for H_2 generation by combining CdS and controlled amounts of Ni_xS_y in 80 mL of 0.1 M Na_2S/0.1 M Na_2SO_3. Approximately 2 mg of CdS was used for each run. Before testing, glassware was rinsed with sulfuric acid to remove noble metal impurities that can uncontrollably affect photocatalytic performance. The suspension was degassed under vacuum for 15 min in a 100 mL round bottom flask while stirring. The remaining head space was then purged with N_2. A 0.4 mL gas sample was taken from the purged reactor to ensure that there was negligible oxygen in the flask. The reactor was then sealed and positioned 20 cm away from a 350 W Xenon lamp fitted with a 420 nm long-pass cut-off filter (Newport), which provided an illumination intensity of approximately 1000 W m^{-2}. A 0.4 mL gas sample was obtained through a septum and analyzed for hydrogen content. All gas content analyses were performed using a model 8610C gas chromatograph (SRI Instruments) equipped with thermal conductivity detector. Error bars associated with photocatalytic data are the standard deviations of n = 3 freshly prepared samples.

Materials characterization

Absorbance measurements were collected using a Shimadzu UV-vis 2600 spectrophotometer equipped with an ISR-2600-Plus integrating sphere attachment. Samples for STEM analysis were prepared by first washing and resuspending the catalysts in DI water, followed by drop casting the suspended sample onto a holey carbon film supported on a

copper mesh grid. Samples were structurally characterized using an aberration corrected JEOL JEM-ARM200 CF transmission electron microscope equipped with a high angle annular dark field (HAADF) detector and a Centurion X-ray energy dispersive (XED) spectrometer. The microscope was operated at 80 kV in STEM mode to characterize nanoparticle size, composition, and crystallography, as well as the spatial distribution of CdS, Ni_xS_y and platinum in the photocatalysts. ICP-OES analyses were performed using a Perkin Elmer ICP-OES Optima 2100DV instrument. The samples for ICP-OES analysis were prepared by washing Ni_xS_y nanoparticles post-enzymatic-synthesis and dissolving them in ~1 M HNO_3.

Powder samples for X-ray photoelectron spectroscopy (XPS) were affixed to the sample plate using carbon tape. Measurements were performed using a custom-built SPECS XPS instrument. Charge neutralization was invoked during the analyses using a beam of 2 eV electrons. All spectra were acquired using an Al K_α photon energy of 1486.6 eV, with analysis performed of electrons escaping in a direction normal to the sample surface. The pass energy for all core level scans was 20 eV and the pass energy for survey scans was 70 eV. Core level spectra were fitted using pseudo-Voigt profile components comprised of approximately 20% Lorentzian and 80% Gaussian broadening. In C1s and O1s spectra, the widths of the components were constrained to be equal. In spectra with doublet peaks (Si2p), the relative heights, widths, and energy separation of the peaks were constrained using library values from Thermo's Avantage software.

Conflicts of interest

There are no conflicts to declare.

Acknowledgments

References

1 B. Su, Z. Cao and Z. Shi, *Acc. Chem. Res.,* 2015, **48**, 886-896.

2 J. Ran, J. Zhang, J. Yu, M. Jaroniec and S. Z. Qiao, *Chem. Soc. Rev.,* 2014, **43**, 7787-7812.

3 X. Zhou, H. Sun, H. Zhang and W. Tu, *Int. J. Hydrogen Energy,* 2017, **42**, 11199-11205.

4 Z. Chen, C. Cheng, F. Xing and C. Huang, *New J. Chem.,* 2020, **44**, 19083-19090.

5 Y. Zhang, Z. Peng, S. Guan and X. Fu, *Appl. Catal. B-Environ.,* 2018, **224**, 1000-1008.

6 C. Li, H. Wang, S. B. Naghadeh, J. Z. Zhang and P. Fang, *Appl. Catal. B-Environ.,* 2018, **227**, 229-239.

7 S. Meng, Y. Cui, H. Wang, X. Zheng, X. Fu and S. Chen, *Dalton T.,* 2018, **47**, 12671-12683.

8 N. Herron, Y. Wang and H. Eckert, *J. Am. Chem. Soc.,* 1990, **112**, 1322-1326.

9 Y. Oaki and H. Imai, *J. Mater. Chem.,* 2007, **17**, 316-321.

10 Y. Oaki and H. Imai, *Angew. Chem. Int. Ed.,* 2007, **46**, 4951-4955.

11 L. C. Spangler, J. P. Cline, C. J. Kiely and S. McIntosh, *Nanoscale,* 2018, **10**, 20785-20795.

12 C. D. Curran, L. Lu, C. J. Kiely and S. McIntosh, *J. Mater. Chem. A,* 2018, **6**, 244-255.

13 R. C. Courtney, R. L. Gustafson, S. Chaberek Jr and A. E. Martell, *J. Am. Chem. Soc.,* 1958, **80**, 2121-2128.

14 v. G. Schwarzenbach, *Helv. Chim. Acta,* 1952, **35**, 2344-2359.

15 M. T. Rodgers and P. B. Armentrout, *Acc. Chem. Res.,* 2004, **37**, 989-998.

16 Y. N. Tan, J. Y. Lee and D. I. Wang, *J. Am. Chem. Soc.,* 2010, **132**, 5677-5686.

17 N. Holten-Andersen, M. J. Harrington, H. Birkedal, B. P. Lee, P. B. Messersmith, K. Y. C. Lee and J. H. Waite, *Proc. Natl. Acad. Sci.,* 2011, **108**, 2651-2655.

18 J. Sakizadeh, J. P. Cline, M. A. Snyder, C. J. Kiely and S. McIntosh, *ACS Appl. Nano Mater.,* 2022, .

19 J. Sakizadeh, J. P. Cline, M. A. Snyder, C. J. Kiely and S. McIntosh, *ACS Appl. Mater. Inter.,* 2020, **12**, 42773-42780.

20 L. C. Spangler, J. P. Cline, J. D. Sakizadeh, C. J. Kiely and S. McIntosh, *Green Chem.,* 2019, **21**, 4046-4054.

21 V. Vij, S. Sultan, A. M. Harzandi, A. Meena, J. N. Tiwari, W. Lee, T. Yoon and K. S. Kim, *ACS Catal.,* 2017, **7**, 7196-7225.

22 L. Michaelis and E. G. Barron, *J. Biol. Chem.,* 1929, **83**, 191-210.

23 J. M. White, R. A. Manning and N. C. Li, *J. Am. Chem. Soc.,* 1956, **78**, 2367-2370.

24 L. Sun, C. Liu, C. Liao and C. Yan, *J. Mater. Chem.,* 1999, **9**, 1655-1657.

25 S. E. Wark, C. Hsia and D. H. Son, *J. Am. Chem. Soc.,* 2008, **130**, 9550-9555.

26 X. Yin, M. Shi, J. Wu, Y. Pan, D. L. Gray, J. A. Bertke and H. Yang, *Nano Lett.,* 2017, **17**, 6146-6150.

27 W. Morris, S. Wang, D. Cho, E. Auyeung, P. Li, O. K. Farha and C. A. Mirkin, *ACS Appl. Mater. Inter.,* 2017, **9**, 33413-33418.

28 K. A. Colwell, M. N. Jackson, R. M. Torres-Gavosto, S. Jawahery, B. Vlaisavljevich, J. M. Falkowski, B. Smit, S. C. Weston and J. R. Long, *J. Am. Chem. Soc.,* 2021, **143**, 5044-5052.

29 L. Huelsenbeck, H. Luo, P. Verma, J. Dane, R. Ho, E. Beyer, H. Hall, G. M. Geise and G. Giri, *Cryst. Growth Des.,* 2020, **20**, 6787-6795.

30 J. Lema, J. A. Ortega, J. D. Martínez, M. L. Araujo, F. Brito, E. Del Carpio, L. Hernández and V. Lubes, *J. Solution Chem.,* 2015, **44**, 2144-2153.

31 N. Karbanee, R. P. Van Hille and A. E. Lewis, *Ind. Eng. Chem. Res.,* 2008, **47**, 1596-1602.

32 X. Jiang, Y. Xie, J. Lu, L. Zhu, W. He and Y. Qian, *Adv. Mater.,* 2001, **13**, 1278-1281.

33 M. Triest, G. Bussière, H. Bélisle and C. Reber, *J. Chem. Educ.,* 2000, **77**, 670.

34 L. I. Katzin, *J. Chem. Phys.,* 1950, **18**, 789-791.

35 P. G. Bruinenberg, G. De Roo and G. Limsowtin, *Appl. Environ. Microbiol.,* 1997, **63**, 561-566.

36 P. J. Desrochers, D. S. Duong, A. S. Marshall, S. A. Lelievre, B. Hong, J. R. Brown, R. M. Tarkka, J. M. Manion, G. Holman and J. W. Merkert, *Inorg. Chem.,* 2007, **46**, 9221-9233.

37 M. Zhou, J. Ding, L. Guo and Q. Shang, *Anal. Chem.,* 2007, **79**, 5328-5335.

38 C. Steegborn, T. Clausen, P. Sondermann, U. Jacob, M. Worbs, S. Marinkovic, R. Huber and M. C. Wahl, *J. Biol. Chem.,* 1999, **274**, 12675-12684.

39 Z. Yang, L. Lu, C. J. Kiely, B. W. Berger and S. McIntosh, *Ind. Eng. Chem. Res.,* 2016, **55**, 11235-11244.

40 T. Chiku, D. Padovani, W. Zhu, S. Singh, V. Vitvitsky and R. Banerjee, *J. Biol. Chem.,* 2009, **284**, 11601-11612.

41 N. E. Good, G. D. Winget, W. Winter, T. N. Connolly, S. Izawa and R. M. Singh, *Biochemistry,* 1966, **5**, 467-477.

42 G. R. Hedwig, J. R. Liddle and R. D. Reeves, *Aust. J. Chem.,* 1980, **33**, 1685-1693.

43 J. W. Bunting and K. M. Thong, *Can. J. Chem.,* 1970, **48**, 1654-1656.

44 M. A. Voelklein, R. O'Shea, A. Jacob and J. D. Murphy, *Energy,* 2017, **121**, 185-192.

45 J. Grau and M. Akinc, *J. Am. Ceram. Soc.,* 1996, **79**, 1073-1082.

46 Y. Xu and M. A. Schoonen, *Am. Mineral.,* 2000, **85**, 543-556.

47 M. Liu, Y. Chen, J. Su, J. Shi, X. Wang and L. Guo, *Nat. Energy,* 2016, **1**, 1-8.

48 Z. Zhang, M. Wang, H. Zhou and F. Wang, *J. Am. Chem. Soc.,* 2021, **143**, 6533-6541.

49 C. Panda, P. W. Menezes, S. Yao, J. Schmidt, C. Walter, J. N. Hausmann and M. Driess, *J. Am. Chem. Soc.,* 2019, **141**, 13306-13310.

50 B. Yan, D. Krishnamurthy, C. H. Hendon, S. Deshpande, Y. Surendranath and V. Viswanathan, *Joule,* 2017, **1**, 600-612.

51 D. M. Poirier and J. H. Weaver, *Surf. Sci. Spectra,* 1993, **2**, 249-255.

52 D. G. Castner, K. Hinds and D. W. Grainger, *Langmuir,* 1996, **12**, 5083-5086.

53 W. Zhang, H. Wang, J. Jiang, Z. Sui, Y. Zhu, D. Chen and X. Zhou, *ACS Catal.,* 2020, **10**, 12932-12942.

54 Y. Xu, W. Tu, S. Yin, M. Kraft, Q. Zhang and R. Xu, *Dalton T.,* 2017, **46**, 10650-10656.

55 B. Weng, M. Qi, C. Han, Z. Tang and Y. Xu, *ACS Catal.,* 2019, **9**, 4642-4687.

56 X. Zhao, J. Feng, J. Liu, W. Shi, G. Yang, G. Wang and P. Cheng, *Angew. Chem. Int. Ed.,* 2018, **130**, 9938-9942.

57 P. Wang, X. Zhang, J. Zhang, S. Wan, S. Guo, G. Lu, J. Yao and X. Huang, *Nat. Commun.,* 2017, **8**, 1-9.

58 W. Zhang, Y. Wang, Z. Wang, Z. Zhong and R. Xu, *Chem. Commun.,* 2010, **46**, 7631-7633.

59 L. Y. Kunz, B. T. Diroll, C. J. Wrasman, A. R. Riscoe, A. Majumdar and M. Cargnello, *Energy Environ. Sci.,* 2019, **12**, 1657-1667.

60 J. Wang, H. Hu, H. Zhang, J. Zhao, X. Li, Z. Song, J. Ding, Y. Deng, X. Han and W. Hu, *Energy Fuels,* 2021, **35**, 6483-6503.

61 B. Ma, X. Wang, K. Lin, J. Li, Y. Liu, H. Zhan and W. Liu, *Int. J. Hydrogen Energy,* 2017, **42**, 18977-18984.

62 D. Zhao, B. Sun, X. Li, L. Qin, S. Kang and D. Wang, *RSC Adv.,* 2016, **6**, 33120-33125.

63 S. Cao and L. Piao, *Angew. Chem. Int. Ed.,* 2020, **59**, 18312-18320.

64 Z. Wang, T. Hisatomi, R. Li, K. Sayama, G. Liu, K. Domen, C. Li and L. Wang, *Joule,* 2021, **5**, 344-359.

65 M. Melchionna and P. Fornasiero, *ACS Catal.,* 2020, **10**, 5493-5501.

66 R. Dunleavy, L. Lu, C. J. Kiely, S. McIntosh and B. W. Berger, *Proc. Natl. Acad. Sci.,* 2016, **113**, 5275-5280.

67 W. W. Yu, L. Qu, W. Guo and X. Peng, *Chem. Mater.,* 2003, **15**, 2854-2860.

68 P. Acero, J. Cama and C. Ayora, *Chem. Geol.,* 2007, **245**, 219-229.